ORIGINAL PAPER

Confining stress effects on global and local responses of internal erosion in gap-graded cohesionless soils

LiangLiang Zhang[1,2] · Gang Deng[1,3] · Rui Chen[1,2] · ZhiYuan Luo[1,2]

Abstract

Internal erosion may affect soil hydraulic properties, inducing localized deterioration and even failure of hydraulic geo-structures. Soil is always subjected to stress in engineering practice; however, the effect of stress on the internal erosion-induced change in soil hydraulic properties along seepage path has not been thoroughly investigated in the literature. In this study, downward seepage-induced internal erosion tests on gap-graded cohesionless soil were conducted using a triaxial permeameter with measurable local hydraulic gradients and deformations. Effects of confining stress on global and local responses of internal erosion were investigated regarding global and local hydraulic gradients and soil deformations as well as eroded fine particles. The results show that the development of seepage velocity during internal erosion exhibits a two-stage linear progression with increasing applied hydraulic gradient under lower confining stress, while it exhibits a single-stage linear progression under higher confining stress. As confining stress increases, both initiation and failure hydraulic gradients are significantly increased, and the onset of the nonuniform distribution of local hydraulic gradients is delayed. Higher confining stress leads to a lower cumulative loss of fine particles and a smaller volume shrinkage, concurrently decreasing the degree of the nonuniform distribution of local hydraulic gradients. Spatial nonuniformity of local hydraulic conductivity and deformations indicates that specimens become more heterogeneous due to the migration of fine particles. Furthermore, although specimens subjected to confining stress exhibit volume shrinkage during internal erosion, the post-erosion void ratio of specimens increases due to the dominant effect of fine particles loss on soil pores.

Keywords Gap-graded cohesionless soil · Internal erosion · Confining stress · Global · Local responses

Introduction

Internal erosion involves selective detachment and progressive migration of finer particles through the voids of the soil skeleton formed by coarser particles under seepage flow (Chang and Zhang 2013a). This phenomenon is widely observed in gap-graded cohesionless soils due to a deficiency in the particle size distribution of the soils (Moffat and Fannin 2006; Ke and Takahashi 2012; Liang et al. 2017; Deng et al. 2020). For soil susceptible to internal erosion, once the fine particles within the soil are eroded and migrated, the local change in hydraulic properties of the soil may change accordingly, such as porosity, permeability, and volume (Chang and Zhang 2011; Ke and Takahashi 2014a; Liang et al. 2017; Zhang et al. 2019). Consequently, internal erosion may induce localized deterioration and even catastrophic failure of the hydraulic geo-structures and their foundations formed by gap-graded cohesionless soils (Richards and Reddy 2007; Zhang et al. 2019; Liu et al. 2019; Yuan and Che 2022). For example, the sudden local surface settlement of the Esfarayen Earth-fill Dam might be attributed to the alterations in hydraulic properties of the core wall of the dam induced by internal erosion (Razavi et al. 2020). Prasomsri and Takahashi (2020) and Huang et al. (2021) also found that an excessive increase in local hydraulic gradients and the local heterogeneity of soil might be regarded as evidence of soil structure becoming

✉ Rui Chen
  cechenrui@hit.edu.cn

1 School of Civil and Environmental Engineering, Harbin Institute of Technology, Shenzhen, Shenzhen 518055, China

2 Guangdong Provincial Key Laboratory of Intelligent and Resilient Structures for Civil Engineering, Harbin Institute of Technology, Shenzhen, Shenzhen 518055, China

3 State Key Laboratory of Simulation and Regulation of Water Cycle in River Basin, China Institute of Water Resources and Hydropower Research, 20 West Chegongzhuang Rd., Haidian District, Beijing 100048, China

unstable due to internal erosion. Therefore, a further understanding of the global and local responses of internal erosion in soils is imperative and significant due to the localization and harmfulness of internal erosion.

Over the last decades, numerous experimental studies on internal erosion have been conducted by various researchers. Relevant studies showed that internal erosion was affected by the physical properties (Kézdi 1979; Moffat and Fannin 2006; Wan and Fell 2008; Zhong et al. 2018; Tian et al. 2020; Liu et al. 2021) and the hydraulic loading condition (Pachideh and Hosseini 2019; Zhou et al. 2018; Benamar et al. 2019; Li et al. 2020) of soil. In most of these studies, the internal erosion tests were carried out using conventional rigid-wall permeameters, and the stress state of soil was not considered in the tests (Moffat and Fannin 2006; Wan and Fell 2008; Zhong et al. 2018; Benamar et al. 2019; Liu et al. 2021). However, the soil in hydraulic geo-structures is usually subjected to complex stress, and hence, the effect of stress state on internal erosion has recently been highlighted (Bendahmane et al. 2008; Moffat et al. 2011; Chang and Zhang 2013a; Liang et al. 2019; Luo et al. 2013, 2020; Deng et al. 2020; Chen et al. 2021; Huang et al. 2021). For example, Moffat and Fannin (2011) and Chen et al. (2021) found that the initiation hydraulic gradient increased with increasing vertical stress under K_0 stress conditions. Chang and Zhang (2011, 2013a), Ke and Takahashi (2014a), and Liang et al. (2017, 2019) suggested that higher confining stress led to a higher initiation and failure hydraulic gradients of internal erosion. In these studies, the initiation and failure hydraulic gradients (i.e., i_{in} and i_f) are defined as the hydraulic gradient when fine particles begin to be discharged and the one when the soil specimen cannot sustain a further increased hydraulic gradient, respectively.

Furthermore, as suggested by Moffat and Fannin (2006, 2011), Israr and Indraratna (2019), Deng et al. (2020), and Chen et al. (2021), the localization of internal erosion due to the migration of fine particles was reported by measuring local hydraulic gradients under K_0 stress conditions. In light of internal erosion tests with different stress states, Ke and Takahashi (2014a), Sato and Kuwano (2015, 2018), Prasomsri and Takahashi (2020), and Kuwano et al. (2021) observed the local change in soil hydraulic properties by measuring the deformations and post-erosion particle size distribution of soil. Although the above experimental approaches have advantages for studying the spatial or temporal characteristics of internal erosion, hitherto, they have rarely focused on the global and local responses of internal erosion under triaxial stress, particularly from the perspective of the local hydraulic gradients. Therefore, the focus of this study is the effects of confining stress on the global and local responses of internal erosion by measuring local hydraulic gradients. This study is expected to provide a novel insight into the spatial–temporal variation in the pore

structure of soil and the local heterogeneity of soil along the seepage path induced by the migration of fine particles.

A comprehensive understanding of internal erosion in terms of global and local responses is beneficial to evaluate internal erosion progress, aiding the rehabilitation of distressed hydraulic geo-structures suffering from internal erosion. This study aims to experimentally investigate the effects of confining stress on global and local responses of internal erosion in gap-graded cohesionless soils. Firstly, a series of internal erosion tests along vertical seepage direction under different confining stresses was conducted using a triaxial permeameter with measurable local hydraulic gradients and soil deformations. During the internal erosion process, global and local hydraulic gradients and volumetric and local deformations as well as cumulative loss of fine particles were measured as indicators to evaluate global and local responses of internal erosion. Subsequently, the pattern of internal erosion progression under different confining stresses was investigated by comparing the seepage velocity of soil specimens. Finally, by comparing the evaluation indicators, the effects of confining stress on the global and local responses of internal erosion were discussed.

Triaxial permeameter, material, and program

Triaxial permeameter

The triaxial permeameter in this study allows the independent control of hydraulic gradient and stress state for investigating the development and failure of internal erosion in soils subject to stress. In contrast to conventional devices, this triaxial permeameter has the advantage of being able to capture local hydraulic gradients and local deformations of soil specimens subjected to stress during the internal erosion process. Figure 1 shows a schematic illustration of the triaxial permeameter. It mainly consists of an erosion and axial stress applying system, a confining stress applying system, a pressurized water supply system, a soil–water separation system, a water collection system, and a data acquisition system. A brief description of each component is presented here. For a detailed description, please refer to Zhang et al. (2023).

As shown in Fig. 1, the main components of the erosion and axial stress applying system are a permeameter chamber, an axial loading device, a top cap, and a base pedestal. The permeameter chamber can accommodate a cylindrical specimen enclosed with a rubber membrane (i.e., flexible wall) to complete the specimen saturation, consolidation, and internal erosion. The confining stress is controlled by a pressure/volume controller (STDDPC GDS, UK) in this study. The perforated plates I and II (referred to as Plates I and II) matching the top cap and base pedestal are placed
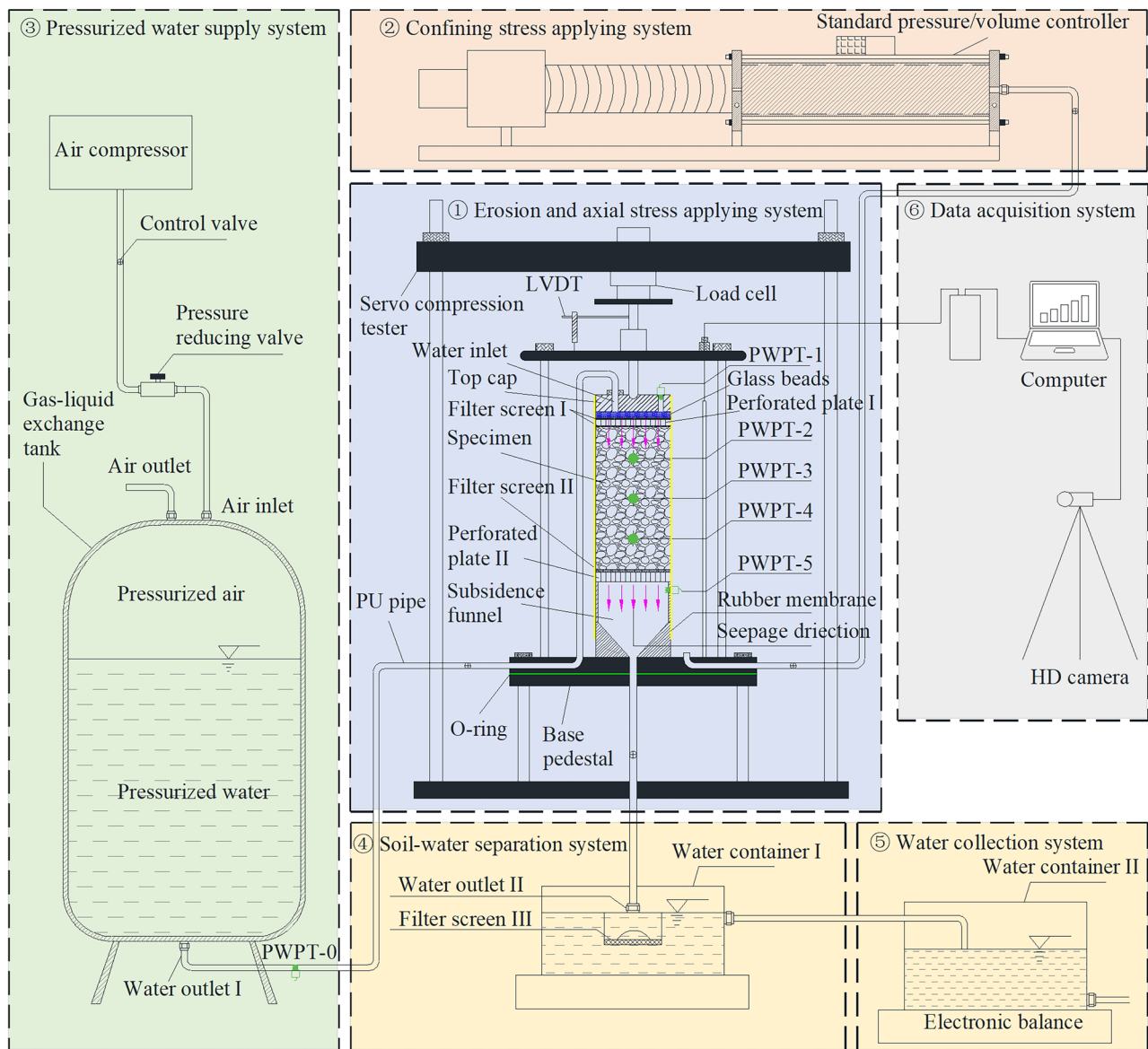
Fig. 1 Schematic diagram of triaxial permeameter

at the top and bottom of the specimen, as shown in Fig. 2. As suggested by Chang and Zhang (2011, 2013a), Ke and Takahashi (2014a, b), and Liang et al. (2017), the area ratio of holes in the perforated plate to the base pedestal (i.e., Plate II) could be 15.0~40.0% in internal erosion tests to avoid the clogging of fine particles and soil arching effect. All perforated plates in this study are designed with hole diameters of 10 mm and center-to-center intervals of 15 mm between any two adjacent holes (see Fig. 2), as suggested by Chang and Zhang (2011, 2013a) and Marot et al. (2020). Thus, the calculated area ratio in this study is 31.5%, which is suitable. Filter screen I with an aperture size of 0.075 mm is adhered on the surface of Plate I to prevent fine particles from clogging Plate I. Additionally, filter screen II with an

aperture size of 1.18 mm is adhered on the surface of Plate II, as suggested by Fannin and Moffat (2006) and Pachideh and Hosseini (2019). This aperture size is 6.2 times the d_{f85} of fine fraction and 5.6 times the maximum particle size of fine fraction (i.e., 0.212 mm), respectively. Thus, in this study, filter screen II can hold coarse particles and allow the passing of fine particles.

The pressurized water supply system mainly consists of an air compressor, a precision reducing valve, and a gas–liquid exchange tank with a 400-l capacity, as shown in Fig. 1. The hydraulic gradient is applied by controlling water pressures at water inlet, while the water pressure at water outlet II is kept at atmospheric pressure. The pressure at the water inlet is regulated by the pressurized water

Fig. 2 Details of the top cap, base pedestal, perforated plates I and II in triaxial permeameter

(a) Details of the top cap and perforated plate I

(b) Details of the base pedestal and perforated plate II
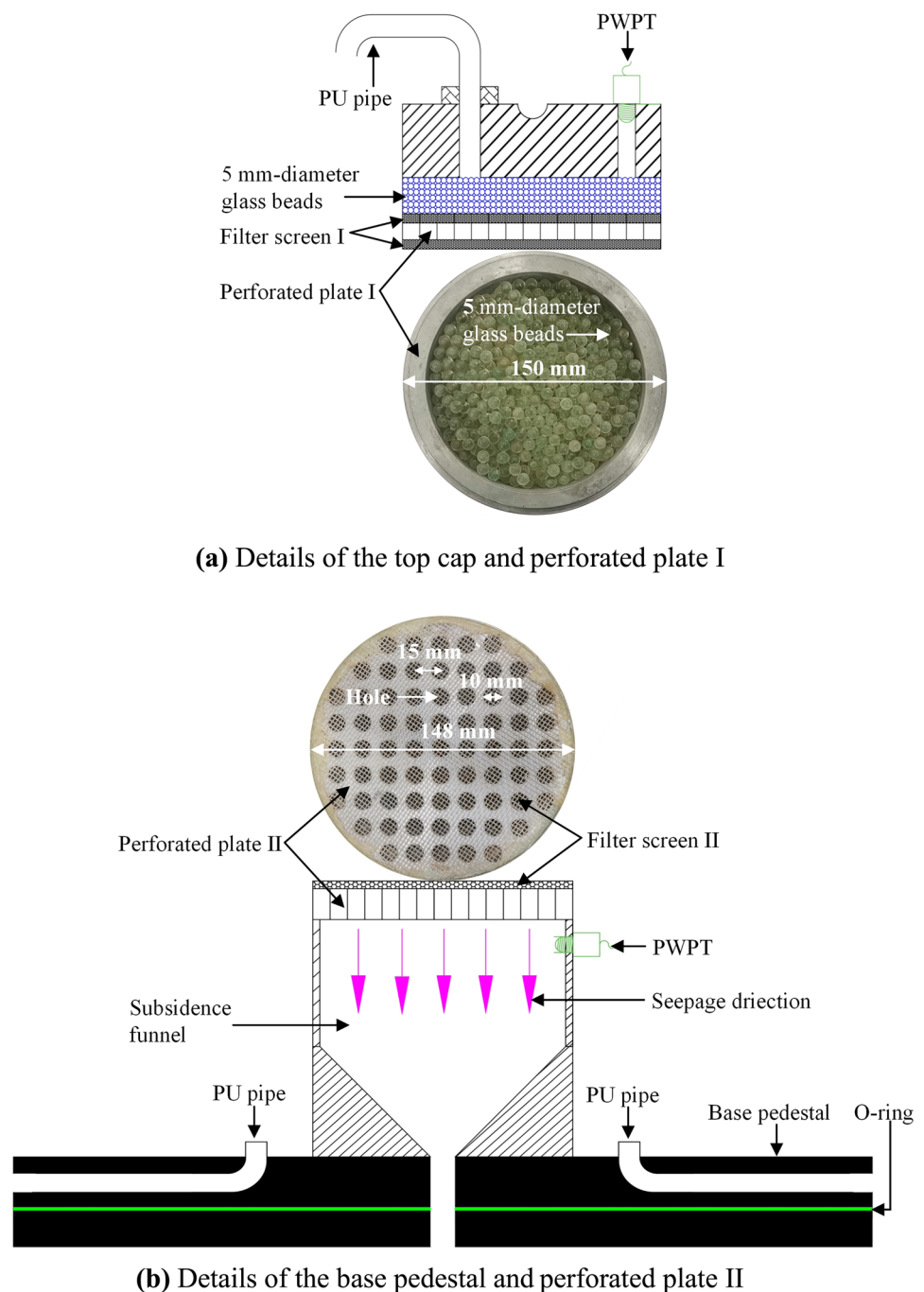
supply system. The maximum applied water pressure in this study can be up to 600 kPa.

The soil–water collection system lies at the bottom of the permeameter chamber, which consists of a drainage funnel, a water container, a filter screen, and an electronic balance (see Fig. 1). Before the outflow from the water outlet II enters the water container, it passes a filter screen III with an aperture size of 0.075 mm, which is set above the water container to collect eroded fine particles. The eroded fine particles can be removed from filter screen III before the applied hydraulic

gradient is increased to the next desired value and dried in an oven to obtain their dry mass. Prior to this step, a new filter screen should be replaced above the previous one to avoid any loss of the eroded particles. The maximum mass of the eroded fine particles is approximately 1% of the mass of collected water under the failure hydraulic gradient for all tests. Hence, the effect of eroded fine particles on the determined seepage velocity is negligible in this study.

As shown in Fig. 1, the data acquisition system includes five pore water pressure transducers (PWPTs) and a

high-definition camera. The measurement range of PWPT is from 0 to 100 kPa with a precision of 0.1% full scale (FS). Among them, with flexible membrane perforation technique, three PWPTs (referred to as PWPT-2 ~ PWPT-4) are installed equidistantly (i.e., the spacing of 7.5 mm, see Fig. 3) at the side surface of the specimen to capture local hydraulic gradients along the seepage path. Readers interested in further details of the membrane perforation technique are referred to Chen et al. (2021). PWPT-1 and PWPT-5 are installed on the top and bottom of the soil specimen (see Fig. 1) to obtain the global hydraulic gradient (i_g) across the specimen. In other words, $i_g = \Delta P_{15}/(\gamma_w \cdot H)$, where ΔP_{15} is the pressure difference between PWPT-1 and PWPT-5; γ_w is the unit weight of water; and H is the height of the specimen. The photographs of specimens are taken every minute to obtain local deformations using a photographic method proposed by Chen et al. (2017). The brief procedure of the photographic method is that the locations of reference points on gridlines of specimens (see Fig. 3) are traced at different times. Hence, the captured pixels on a photographic image can be converted to the radial and axial deformations of specimens using the quantized relationship between the pixels and grid size. The volumetric strain of specimens is monitored by the pressure/volume controller during the internal erosion process.

Test material

Gap-graded soils, such as sandy gravels, are especially vulnerable to internal erosion due to their deficiency of particle size distribution (Skempton and Brogan 1994; Ke and Takahashi 2012; Khaksar Najafi and Eslami 2015). It is generally accepted that the gap-graded soils may be found at earth dams that have suffered from years of internal erosion or at construction sites with substandard procedures of particle mixing (Milligan 2003; Ke and Takahashi 2014a; Benamar et al. 2019). Artificial gap-graded soil is used in this study. The test soil is the binary mixtures of quartz sands with fine fraction "F" and coarse fraction "C" using a ratio of 3:7 by weight (F:C = 3:7). The particle size distribution of the test soil and the quartz sands with different particle sizes are shown in Fig. 4. Physical properties of the test soil are summarized in Table 1. The coarse fraction is regarded as the soil-skeleton particle, and the fine fraction is considered as the erodible fine particles through the voids of the soil skeleton formed by coarse particles. According to Unified Soil Classification System (ASTM D2487-17 2017), the soil is classified as poorly graded sand (SP). Referring to the geometric criteria proposed by Kézdi (1979), Kenney and Lau (1985), Burenkova et al. (1993), and Mao (2005),
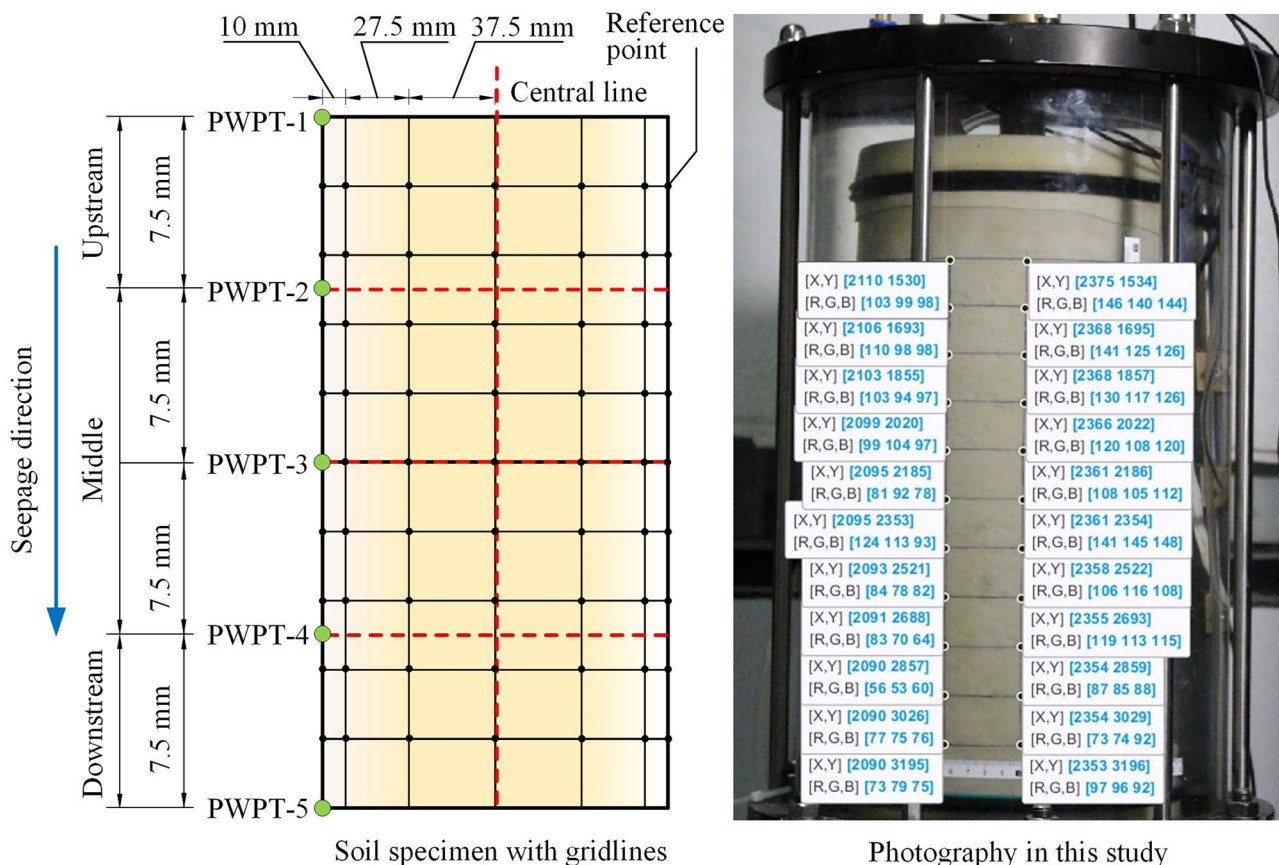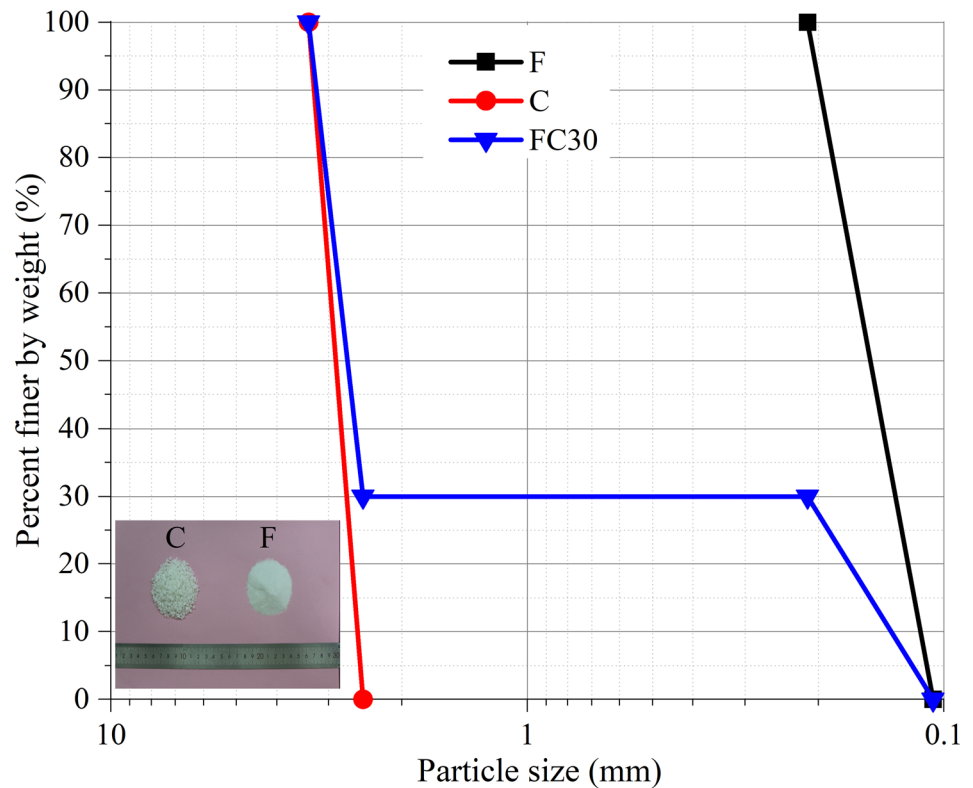

Fig. 3 Application of the photographic method on the specimen in this study

Fig. 4 Particle size distribution of test soil

the test soil is regarded as internally unstable (see Table 2), implying that such soil is susceptible to internal erosion.

Test program

In this study, seven internal erosion tests were performed to investigate the effect of effective confining stress, as shown in Table 3. Vallejo (2001) found that the soil-skeleton structure of binary mixtures was characterized by coarse particles when the coarse particle concentration was greater than 70%, while the fine particles dominated if the coarse particle concentration was less than 40%. Ke and Takahashi (2012) calculated that the maximum mass of fine fraction was approximately 37% for the binary mixtures of quartz sands derived from the geometrical restriction (i.e., the

Table 1 Physical properties of test soil in this study

Physical property	Sand F	Sand C	Test soil
FC (%)	100	0	30
Specific gravity, G_s	2.65	2.65	2.65
Effective particle size, d_{10} (mm)	0.11	2.56	0.13
Median particle size, d_{30} (mm)	0.13	2.73	0.21
Mean particle size, d_{50} (mm)	0.15	2.89	2.70
Constrained particle size, d_{60} (mm)	0.16	2.98	2.82
Maximum void ratio, e_{max}	1.31	1.05	0.75
Minimum void ratio, e_{min}	0.71	0.70	0.38
Coefficient of uniformity, C_u	1.45	1.16	21.69
Coefficient of curvature, C_c	0.96	0.98	0.12

volume of fine particles should be less than that of the voids between coarse particles). According to the calculation method suggested by Ke and Takahashi (2012), the maximum mass of fine fraction was approximately 38.2% for the test soil in this study. In addition, according to the General Design and Construction Considerations for Earth and Rock-Fill Dams (US Army Corps of Engineers, EM 1110-2-2300 2004), foundation sands should have an adequate density (at least 70% relative density) to enhance the stability of soil structure. Thus, as shown in Table 3, the initial fine content (FC, i.e., the mass ratio of fine particles to total weight of soil specimen) of 30% and the initial relative density (D_r) of 75% were adopted in all tests. The applied effective confining stress was 25, 50, 100, 150, and 200 kPa, which approximately mimicked the self-weight stress of soil mass at depths of 2.5, 5, 10, 15, and 20 m, respectively. Furthermore, to demonstrate test repeatability, the specimens FC30-D75-C100-R1 and FC30-D75-C100-R2 were tested under the same initial conditions as the specimen FC30-D75-C100.

Test procedure

All tests are mainly divided into the following four steps: (1) specimen preparation and compaction, (2) specimen saturation, (3) specimen consolidation under effective confining stress, and (4) internal erosion process, i.e., application of hydraulic gradient.

Table 2 Assessment of internal stability of test soil

Criteria	The soil is internally stable if	Value	Test soil
Kézdi (1979)	$(d_{c15}/d_{f85})_{max} \leq 4$	13.68	U
Kenney and Lau (1985)	$(H/F)_{min} \geq 1, (0 < F < 20\%)$	0.49	U
Burenkova (1993)	$0.76\log(h'') + 1 < h' < 1.86\log(h'') + 1$	–	U
Mao (2005)	$4P_f(1-n) \geq 1$	0.81	U
Chang and Zhang (2013b)	$G_r < 0.3P_f, (10\% \leq P_f \leq 35\%)$	11.70	U
Experimental result	–	–	U

U means unstable; d_{c15} is the particle size finer than which the soil weight by percentage is 15% for the coarse fraction; d_{f85} is the particle size finer than which the soil weight by percentage is 85% for the fine fraction; F is the weight fraction of the soil finer than size d; H is the weight fraction of the soil in the size ranging from d to $4d$; $h' = d_{90}/d_{60}$; $h'' = d_{90}/d_{15}$; d_x means the particle size finer than which the soil weight by percentage is $x\%$; n is the porosity ($n = 0.321$ in this study, derived from Table 3, i.e., initial void ratio), and P_f is the fine content by weight in soil; $G_r = d_{max}/d_{min}$, d_{max}, and d_{min} is the maximal and minimal particle sizes characterizing the gap in grading curve

Specimen preparation

The specimen is 150 mm in diameter and 300 mm in height in this study. According to the ASTM D4767-11 (2011), the reconstituted specimen may be prepared by compacting material in at least six layers. Additionally, as suggested by Chang and Zhang (2013a) and Ke and Takahashi (2014a), the specimen was compacted in eight layers and ten layers during specimen preparation, respectively. Thus, the specimen is compacted in ten layers, and the thickness of each layer is 30 mm to ensure the specimen uniformity during preparation. The relative density of the specimen is 75%, which corresponds to a dry density of 1.8 g/cm³ in this study; hence, a dry soil material and deaired water required for each layer can be calculated in advance and fully mixed. First, the mixed soil material is poured into a split mold and compacted to reach a target thickness. After specimen compaction, the mold is detached, and a flexible membrane with the drawn gridlines is put onto the specimen. Second, PWPT-2 ~ PWPT-4 are installed and attached to the side surface of the specimen using a membrane perforation technique. Finally, the triaxial permeameter chamber is mounted on the base pedestal, thereby completing specimen preparation.

Specimen saturation

After specimen preparation, a differential water-head method is adopted to saturate the specimen, as suggested by Chang and Zhang (2011, 2013a). During saturation, a low confining stress (i.e., 20 kPa) is applied to prevent the collapse of the specimen and any leakage between the specimen and the membrane, as suggested by Bendahmane et al. (2008). To ensure a good saturation result, carbon dioxide is slowly injected into the specimen from the water outlet II to displace the air within the specimen (approximately 8–10 h in this study). Subsequently, deaired water is gradually infiltrated into the specimen from water outlet II by increasing the water-head. Note that the inflow rate should be sufficiently slow to avoid particle segregation within the specimen. The supply process of deaired water lasts (approximately 10–12 h in this study) until the inflow rate equals the outflow rate. The above saturation procedure can lead to the Skempton B-value being greater than 0.9, as measured in this study.

Consolidation under applied confining stress

After saturation, the specimen consolidation is conducted using a confining stress applying system under the desired

Table 3 Test program

Specimen	Initial relative density, Dr (%)	Initial FC (%)	Effective confining stress, (kPa)	Initial void ratio	Post-consolidation void ratio
FC30-D75-C25	75	30	25	0.472	0.470
FC30-D75-C50	75	30	50	0.472	0.468
FC30-D75-C100	75	30	100	0.472	0.462
FC30-D75-C100-R1	75	30	100	0.472	0.462
FC30-D75-C100-R2	75	30	100	0.472	0.462
FC30-D75-C150	75	30	150	0.472	0.457
FC30-D75-C200	75	30	200	0.472	0.450

effective confining stress (see Table 3) to approximately mimic the self-weight stress of soil mass. Note that the effective confining stress gradually increases up to the desired value at fairly small increments (i.e., 1 kPa/min) by a standard pressure/volume controller (see Fig. 1) to avoid the migration of soil particles. The water inlet of the triaxial permeameter is opened when the effective confining stress is incrementally increased to the desired value. During consolidation, the volume of pore water drained from the specimen can be measured to obtain the post-consolidation void ratio of the specimen. The consolidation stage is completed when the PWPTs become stable (approximately 12 h in this study).

Application of a hydraulic gradient

After consolidation, a hydraulic gradient is applied to the specimen by increasing the water pressure at the water inlet. The applied hydraulic gradient is increased step by step and maintained for more than 10 min for each step, as suggested by Chang and Zhang (2011). PWPTs are recorded every 3 s by a data logger to obtain the change in pore water pressure during tests. Outflow weight is recorded every 10 s using an electronic balance to capture the variations in seepage velocity. If fine particles are observed in the outflow, the applied hydraulic gradient is kept constant until no particle loss is observed. Subsequently, the applied hydraulic gradient is increased to the next desired value. When the applied hydraulic gradient reaches a threshold value, the seepage velocity increases rapidly, flushing out abundant fine particles from the specimen. After that, the specimen cannot sustain any further increase in the applied hydraulic gradient. Hence, as reported by Liang et al. (2017) and Deng et al. (2020), the threshold value is termed the failure hydraulic gradient (i_f), and the observed phenomenon can be regarded as the macroscopic manifestation of the internal erosion failure of the specimen in this study. Afterward, the internal erosion tests are terminated.

Results and analysis

Test repeatability

As suggested by Richards and Reddy (2010) and Liang et al. (2017), test repeatability was evaluated by the coefficient of variation (C_v) of the characteristic hydraulic parameters, such as the initiation and failure hydraulic gradients (i_{in} and i_f), the initial hydraulic conductivity (k_0), and the average hydraulic conductivity (k_{av}). Furthermore, Richards and Reddy (2010) suggested that the C_v value of 10% should be used as a threshold value to evaluate test repeatability. The C_v is defined as follows:

$$C_v = \frac{\sigma}{\mu} \tag{1}$$

where σ and μ are the standard deviation and the average value of characteristic hydraulic parameters.

According to Eq. (1), test results regarding repeatability are listed in Table 4. Figure 5 shows the development of seepage velocity (v) with the increasing applied hydraulic gradient (i.e., global hydraulic gradient, i_g) for the specimens FC30-D75-C100, FC30-D75-C100-R1, and FC30-D75-C100-R2. From Fig. 5, the development curves of these specimens were nearly identical, and the maximum C_v of seepage velocity was 6% at the different applied hydraulic gradients. Furthermore, from Table 4, the C_v of characteristic hydraulic parameters was within 5%. Thus, this small difference indicated that the test repeatability in this study was satisfactory.

Similarly, Fig. 6 shows the evolution of radial deformation for the specimens FC30-D75-C100, FC30-D75-C100-R1, and FC30-D75-C100-R2 to demonstrate the repeatability of the photographic method (Chen et al. 2017) used in this study. As shown in Fig. 6a, the evolution curves of these specimens were almost the same. Furthermore, from Fig. 6b, the maximum C_v of the radial deformation was within 5% at the different internal erosion times. The small difference indicated that the repeatability of the photographic method was satisfactory in measuring soil deformations.

## Effect of confining stress on pattern of internal erosion progression

Figure 7 shows the internal erosion progression, manifested by the development of seepage velocity (v) with the increasing applied hydraulic gradient under different effective confining stresses. As expected, v increased approximately linearly when i_g was relatively small for each case. The result was consistent with the observations by Liang et al. (2017) and Deng et al. (2020). For the specimens FC30-D75-C25 and FC30-D75-C50, fine particles began to be flushed out when the applied hydraulic gradient reached 0.66 and 0.89,

Table 4 Results of repeatability tests

Specimen	i_{in}	C_v (%)	i_f	C_v (%)	k_0 (cm/s)	C_v (%)	k_{av} (cm/s)	C_v (%)
FC30-D75-C100	1.15		2.27		0.0381		0.0378	
FC30-D75-C100-R1	1.17	0.8	2.46	4.2	0.0392	4.5	0.0375	1.8
FC30-D75-C100-R2	1.15		2.24		0.0423		0.0389	

Fig. 5 Response of the seepage velocity with the global hydraulic gradient in repeatability tests under 100 kPa confining stress
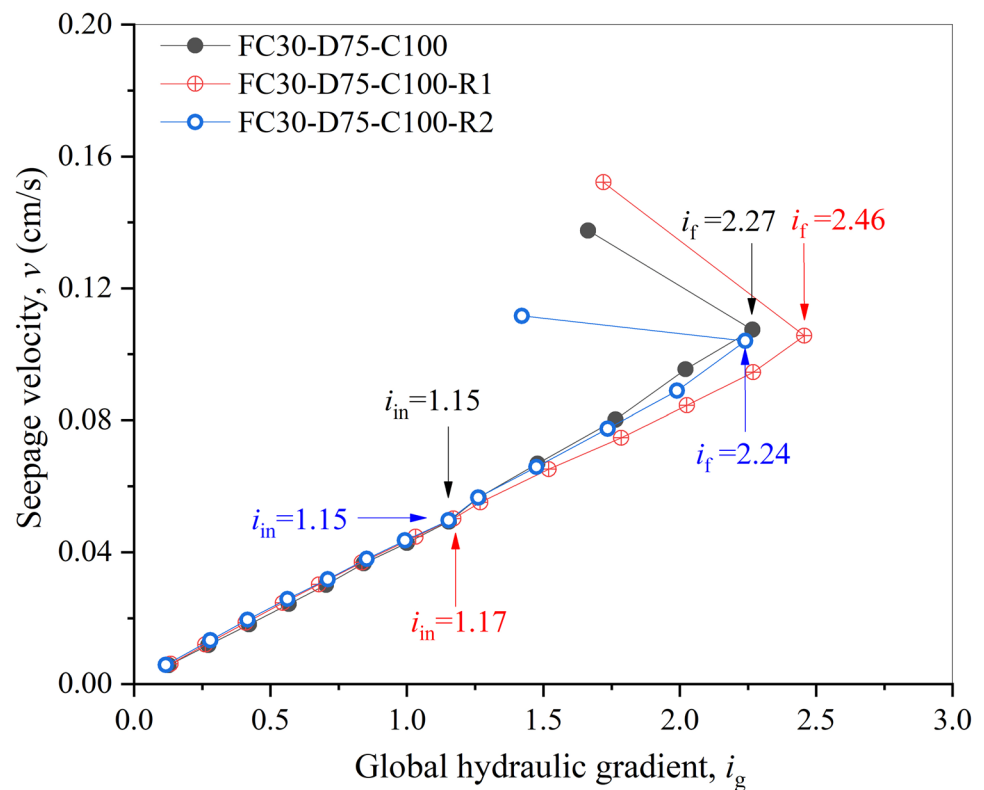
respectively. The observation might be considered a sign of internal erosion initiation, and the corresponding i_g was termed the initiation hydraulic gradient (i_{in}) in this study. According to this observation, the i_{in} for the specimens FC30-D75-C100, FC30-D75-C150, and FC30-D75-C200 were determined to be 1.15, 1.24, and 1.31, respectively.

From Fig. 7, with the increasing applied hydraulic gradient, the development of seepage velocity exhibited the two-stage linear pattern (i.e., solid line segment and dashed line segment in Fig. 7) before failure hydraulic gradients under low effective confining stress (25, 50 kPa). Under high effective confining stress (100, 150, 200 kPa), the increase in seepage velocity consistently exhibited a linear development until failure hydraulic gradient, i.e., the single-stage linear pattern. This observation indicated that the internal erosion progression of gap-graded cohesionless soil was significantly affected by effective confining stress, characterized by the change in the progression pattern with increasing effective confining stress. The reason might be that the size of soil pores became smaller under higher effective confining stress, as evidenced by the decrease in the void ratio of soil specimens (see Table 3). In addition, the interlocking between coarse and fine particles was firmer under higher effective confining stress, leading to greater involvement of fine particles in force chains. As a result, the smaller pores and enhanced constraints might restrict the migration of fine particles, thereby decelerating the development of internal

erosion, exhibiting a stable slope of the v-i_g curve under high effective confining stress (see Fig. 7).

Effect of confining stress on characteristic hydraulic gradients

Figure 8 presents the effect of effective confining stress on characteristic hydraulic gradients (i.e., i_{in} and i_f). Both initiation and failure hydraulic gradients increased nonlinearly with increasing effective confining stress. On the one hand, under low effective confining stress, most fine particles might be freely filled in the voids of the soil skeleton formed by coarse particles and not be involved in force chains due to the small constraints for soil structure. Thus, fine particles might be migrated and discharged easily by seepage force under low effective confining stress, thereby resulting in low initiation hydraulic gradient. On the other hand, the contacts and interlocking among soil particles were enhanced with increasing effective confining stress, exhibiting an enhancement in erosion resistance of soil specimens (Chang and Zhang 2013a; Ke and Takahashi 2014a, b; Liang et al. 2019). As a result, the migration and loss of fine particles within soil pores became more difficult under high effective confining stress, leading to high initiation and failure hydraulic gradients. As evidenced by Chang and Zhang (2013a), the initiation hydraulic gradient increased from 0.87 to 1.77 (i.e., $i_{in, exp}$ in Fig. 8) when

Fig. 6 Results of the photographic method in repeatability tests under 100 kPa confining stress
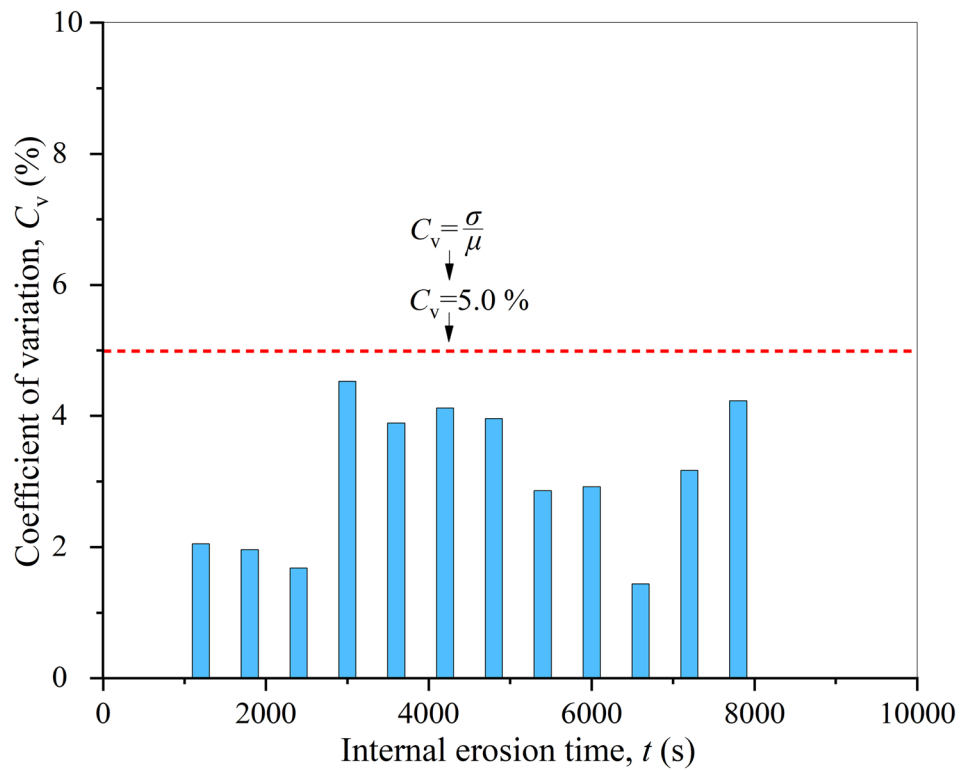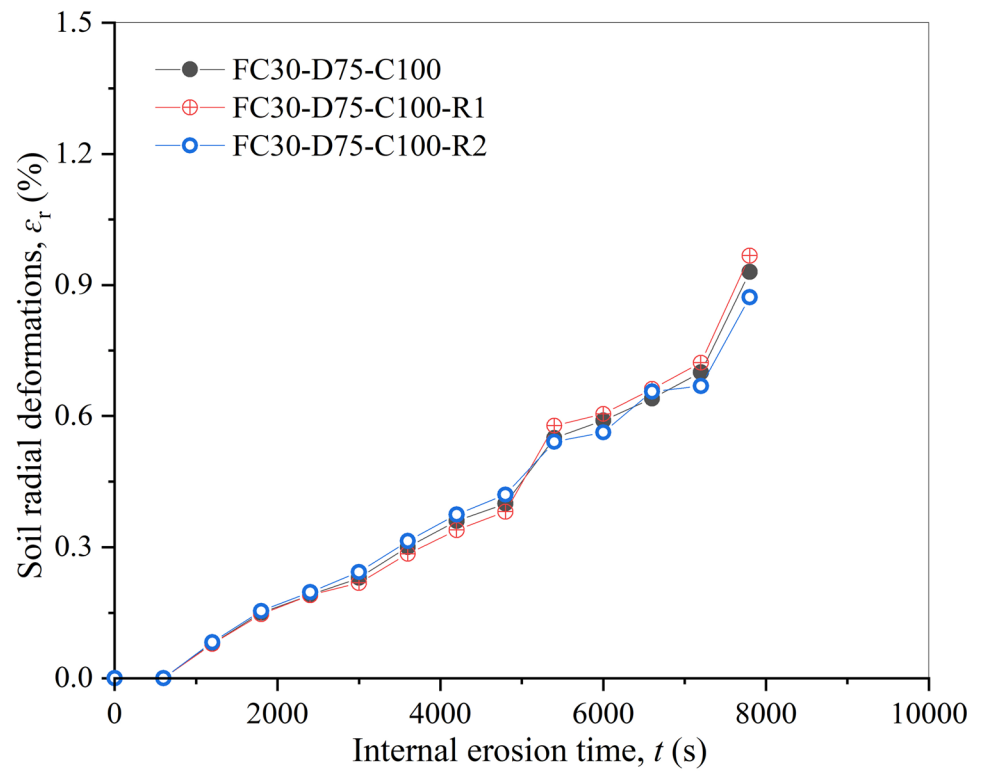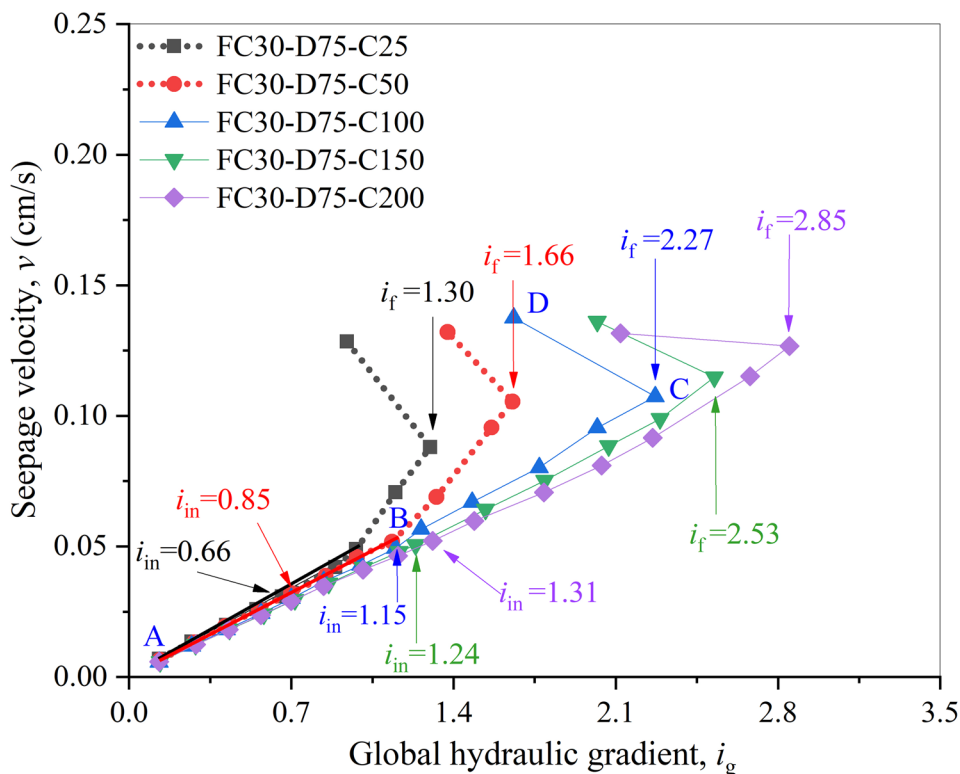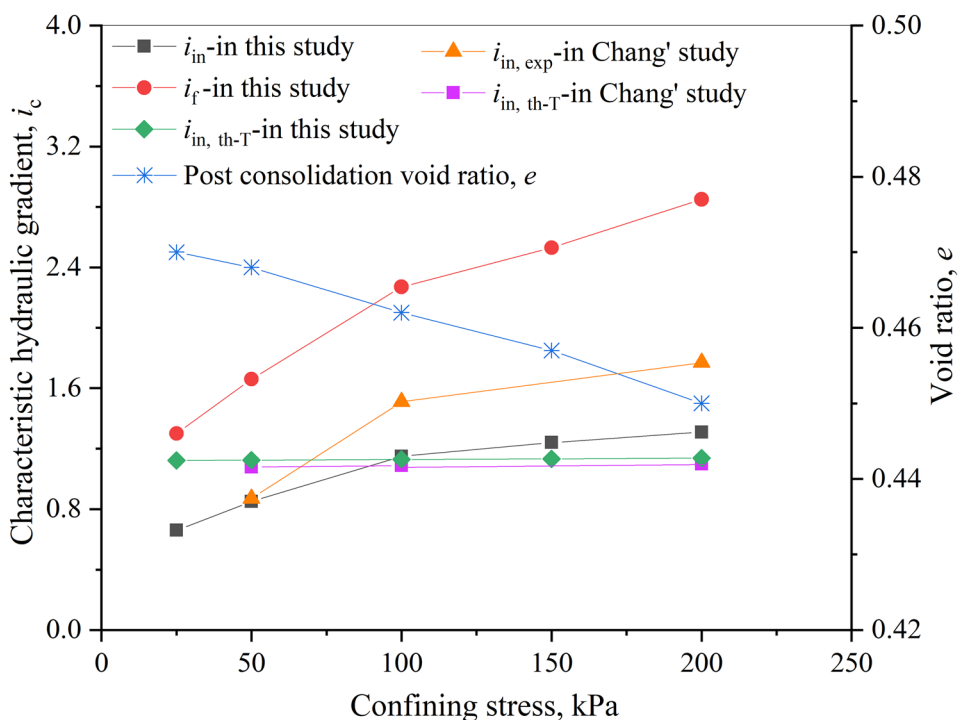
effective confining stress increased from 50 to 200 kPa for gap-graded specimens with 35% FC. They also found that the loss of eroded fine particles decreased with increasing effective confining stress, implying an enhancement in the erosion resistance.

Furthermore, the theoretical initiation hydraulic gradient ($i_{in, th-T}$ in Fig. 8) under no stress could be calculated by Terzaghi's theory (Terzaghi 1939). The $i_{in, th-T}$ for the specimens FC30-D75-C25, FC30-D75-C50, FC30-D75-C100, FC30-D75-C150, and FC30-D75-C200 in this study were

1.122, 1.124, 1.129, 1.133, and 1.138, respectively. Similarly, the $i_{in, th-T}$ in Chang's study were 1.078, 1.088, and 1.098 (see Fig. 8) for soil specimens under effective confining stress of 50, 100, and 200 kPa, respectively. In this study, the $i_{in, th-T}$ increased by only 1.43% as the effective confining stress increased from 50 to 200 kPa, whereas the i_{in} increased by up to 54.11%, as shown in From Fig. 8. Correspondingly, in Chang's study, the $i_{in, th-T}$ increased by only 1.86%, whereas the experimental initiation hydraulic gradient ($i_{in, exp}$ in Fig. 8) increased by up to 103.45%. Additionally, as the effective confining stress increased from 50 to 200 kPa, the void ratio of soil specimens decreased by 3.85% and 4.46% in this study and Chang's study, respectively. The observations might indicate that both initiation and failure hydraulic gradients were significantly affected by effective confining stress. The stress-induced change in initiation and failure hydraulic gradients could not be explained only from the point of view that the increase in stress led to the decrease in soil porosity, and hence, the effect of stress on the contacts and interlocking among soil particles should also be considered.
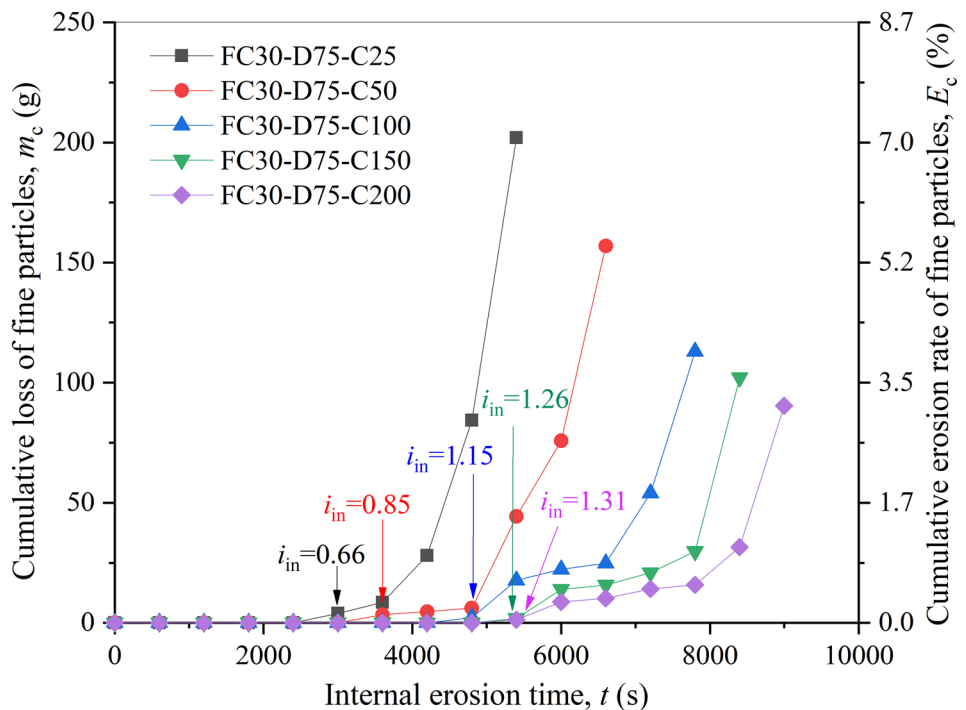
Effect of confining stress on cumulative loss of fine particles

Figure 9 presents the evolution of the cumulative loss (m_c) and erosion rate (E_c) of fine particles with internal erosion time (t) under different effective confining stresses. Note that the cumulative erosion rate of fine particles means the mass ratio of cumulative eroded fine particles to total fine particles of the soil specimen. From Fig. 9, after the internal erosion initiation, the cumulative loss of fine particles increased with internal erosion time under different effective confining stresses, and the degree of loss was more significant at the later stage of the internal erosion process. This finding indicated the nonlinear relationship between the cumulative eroded soil mass and the internal erosion time. Internal erosion tests conducted by Liang et al. (2017) also found a similar observation for gap-graded soil specimens with 25% FC.

Table 5 shows the detailed results regarding the cumulative loss of fine particles during the internal erosion process under different effective confining stresses. From Table 5, compared to the specimen FC30-D75-C25, the cumulative erosion rate for the specimens FC30-D75-C100, FC30-D75-C150, and FC30-D75-C200 decreased by more than 40% at both initiation and failure states of internal erosion. Furthermore, the cumulative eroded soil mass decreased significantly with increasing effective confining stress. Taking the specimens FC30-D75-C25 and FC30-D75-C200 as examples, the effect of effective confining stress on the cumulative loss of fine particles was elaborated. The eroded fine particles began to be flushed out from the specimens FC30-D75-C25 and FC30-D75-C200 when the applied hydraulic gradient increased to 0.66 and 1.31 (i.e., i_{in} in Fig. 9), respectively. The corresponding internal erosion time lasted 3000 s and 5400 s (i.e., t_{in} in Table 5). Under the initiation hydraulic gradient, the E_{in-c} value decreased from 0.14 to 0.04%, with a decreasing range of 71.43%, and the time of the internal erosion initiation was delayed by 1.8

Fig. 9 Effect of confining stress on the cumulative loss and erosion rate of fine particles under different internal erosion times for the specimen with 30% initial fine content

Table 5 Detailed results of cumulative loss of fine particles during the internal erosion process under different confining stresses

Specimen	Internal erosion initiation (i_{in})				Internal erosion initiation to failure ($i_{in} \sim i_f$)			
	$m_{in\text{-}c}$	$E_{in\text{-}c}$	Decrease	t_{in}	$m_{f\text{-}c}$	$E_{f\text{-}c}$	Decrease	t_f
	(g)	(%)	(%)	(s)	(g)	(%)	(%)	(s)
FC30-D75-C25	3.9	0.14	–	3000	202	7.06	–	5400
FC30-D75-C50	3.3	0.12	14.29	3600	156.8	5.48	22.4	6600
FC30-D75-C100	2.1	0.07	50	4800	112.8	3.94	44.19	7800
FC30-D75-C150	1.8	0.06	57.14	5400	102.1	3.57	49.43	8400
FC30-D75-C200	1.3	0.04	71.43	5400	90.4	3.16	55.24	9000

times. During the internal erosion process ($i_g = 0 \rightarrow i_g = i_f$), the $E_{f\text{-}c}$ value for the specimens FC30-D75-C25 and FC30-D75-C200 decreased from 7.06 to 3.16%, with a decreasing range of 55.24%. Correspondingly, the internal erosion time lasted 5400 s and 9000 s (i.e., t_f in Table 5); this is, the time of the internal erosion failure was delayed by 1.7 times. The results indicated that increasing effective confining stress could significantly reduce the loss of fine particles and delay the initiation and failure of internal erosion. This reduction and delay also might imply that the erosion resistance of soil specimens was enhanced.

Discussion of local responses of internal erosion

Development of local hydraulic gradients with increasing applied hydraulic gradient

Local hydraulic gradients can be obtained from the measurements of pore water pressure at points PWPT-1 ~ PWPT-5 (see Fig. 3) in this study. In this figure, $i_{k\text{-}j}$ denotes the hydraulic gradient between points PWPT-k and PWPT-j. For example, $i_{1\text{-}2}$ means the local hydraulic gradient between points PWPT-1 and PWPT-2 (see Fig. 3). Figure 10 shows the development of local hydraulic gradients along the seepage path with the increasing applied hydraulic gradient under different effective confining stresses. From Fig. 10, the development of local hydraulic gradients could be divided into three stages for each case: uniform stage, nonuniform stage, and failure stage.

At the uniform stage (see Fig. 10), the local hydraulic gradients increased approximately linearly when the applied hydraulic gradients were lower than 0.85, 1.15, 1.24, and 1.31 (i.e., i_{in}) for the specimens FC30-D75-C50, FC30-D75-C100, FC30-D75-C150, and FC30-D75-C200, respectively. The local hydraulic gradients along the seepage path were uniformly distributed and were consistent with each other. The result implied that contacts and interlocking among soil particles could not be overcome by seepage forces, and hence, there is no erosion and loss of fine particles at this stage. Accordingly, the pore structure of soil specimens might maintain homogenous at the uniform

distribution stage. This observation was consistent with Ke and Takahashi (2012, 2014a). They found that the local hydraulic conductivities were basically the same due to the integrity and homogeneity of soil specimens before the internal erosion initiation.

At the nonuniform stage (see Fig. 10), since the internal erosion initiation, fine particles might begin to migrate from one location to another location in the voids of the soil skeleton until the rearrangement of all particles reached an equilibrium. As a result, the pore structure was locally altered due to the migration and clogging of movable fine particles at the nonuniform stage. Thus, the local hydraulic gradients at different locations became different, exhibiting a nonuniform distribution along the seepage path. This observation implied that the pore structure along the seepage path might begin to become heterogeneous. Furthermore, the nonuniform distribution of local hydraulic gradients was gradually aggravated with the increasing applied hydraulic gradient. Ke and Takahashi (2014a), Sato and Kuwano (2015, 2018), and Kuwano et al. (2021) characterized the change in pore structure as a small localized collapse, potentially leading to the heterogeneity of soil specimen. Additionally, the decrease in local hydraulic gradient downstream (i.e., $i_{4\text{-}5}$) might be considered a sign of the onset of the nonuniform distribution for each case. For example, the $i_{4\text{-}5}$ decreased from 0.70 to 0.54, 0.85 to 0.46, 1.00 to 0.90, and 1.12 to 1.09 for the specimens FC30-D75-C50, FC30-D75-C100, FC30-D75-C150, and FC30-D75-C200, respectively (see Fig. 10). Similarly, the internal erosion initiation could be characterized by a sudden drop in local hydraulic gradients, as suggested by Moffat and Fannin (2011) and Indraratna et al. (2018).

From Fig. 10, with increasing effective confining stress, the onset of the nonuniform distribution was delayed, and the degree of the nonuniform distribution was decreased correspondingly, implying the enhancement in erosion resistance of soil specimens. On the one hand, as the effective confining stress increased, the void ratio of soil specimens became smaller (see Table 3), resulting in a denser packing of fine particles among the voids of the soil skeleton formed by coarse particles (Ke and Takahashi 2014a). Accordingly,
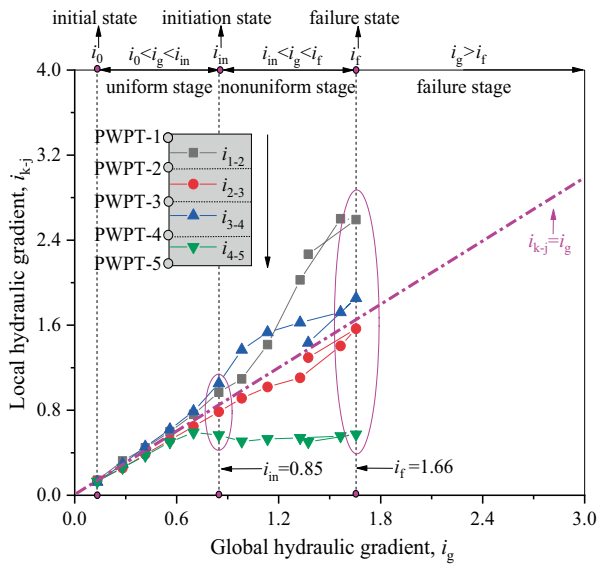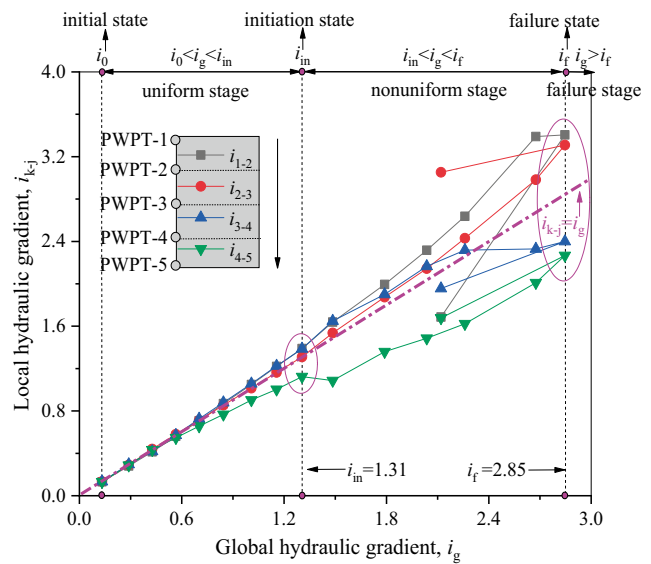
(a) Specimen FC30-D75-C50
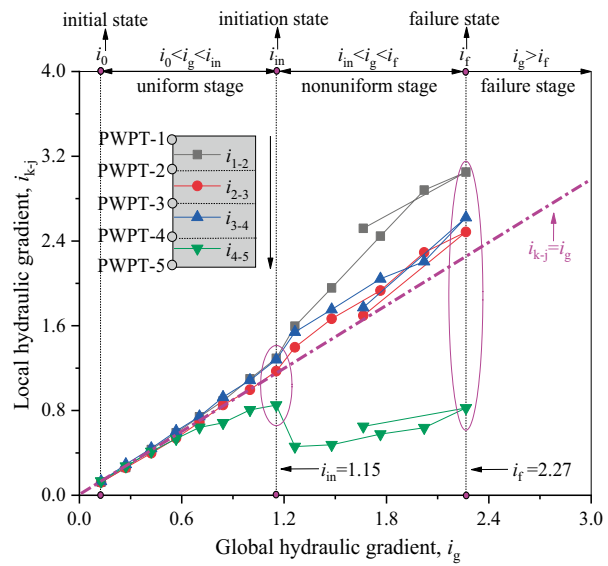
(b) Specimen FC30-D75-C100
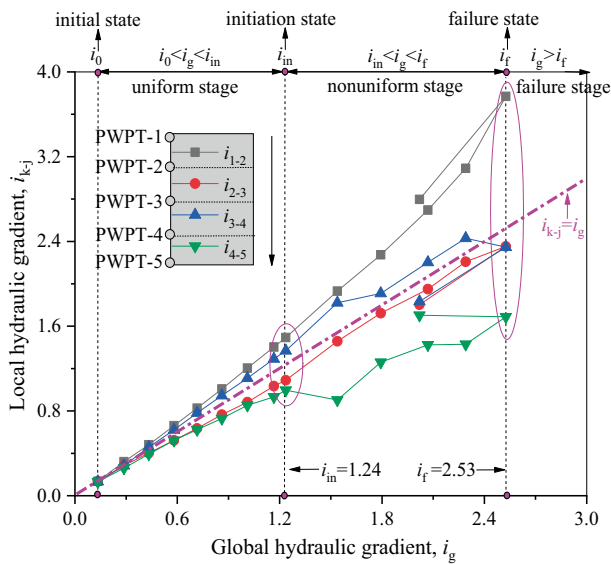
(c) Specimen FC30-D75-C150

(d) Specimen FC30-D75-C200

Fig. 10 Development of local hydraulic gradients with the increasing applied hydraulic gradient under different confining stresses for the specimen with 30% initial fine content

the soil specimen might remain intact and homogeneous for a longer period under higher effective confining stress. On the other hand, with increasing effective confining stress, the soil specimen might become more difficult to erode as most fine particles might be involved in force chains, enhancing the friction and interlocking among soil particles. As a result, fine particles became more difficult to migrate, decreasing the degree of the nonuniform distribution. The erosion zone on the top surface of the soil specimen might serve as a visual

observation, exhibiting a decrease in the erosion zone with increasing effective confining stress, as shown in Fig. 11.

At the failure stage, the internal erosion failure was caused by the significantly increased pore water pressure at the top of the soil specimen (i.e., near the upstream portion) and the profoundly weakened soil structure due to the abundant loss of fine particles. As a result, the local hydraulic gradients along the seepage path could no longer be sustained anymore and dropped suddenly (see Fig. 10). The studies conducted by Israr
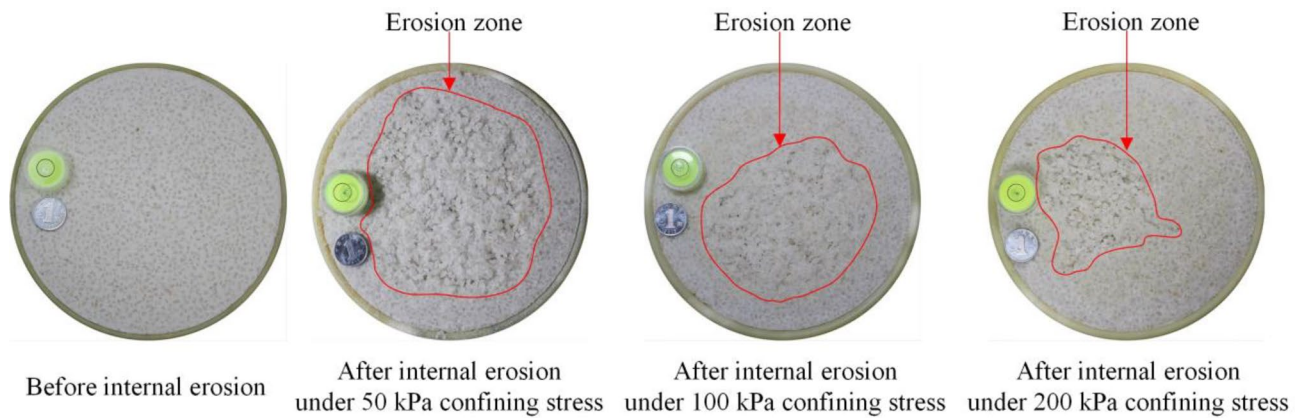
Fig. 11 Erosion zone on top surface of the specimen with 30% initial fine content under different confining stresses

and Indraratna (2019) exhibited the same trend that the occurrence of excessive pore water pressure somewhere within soil specimen might be a cause of internal erosion failure. Huang et al. (2021) also found that the internal erosion failure might be attributed to the excessive increase in local hydraulic gradients.

Spatial and temporal evolution of local hydraulic gradients

Taking the specimen FC30-D75-C100 as an example, the spatial and temporal evolution of local hydraulic gradients along the seepage path during the internal erosion process was specifically interpreted, as shown in Fig. 12. Furthermore, the change in hydraulic conductivity might result from the change in soil pore structure induced by the migration and loss of fines, and this change could be characterized by the evolution of local hydraulic gradients, as suggested by Ke and Takahashi (2014a) and Sato and Kuwano (2015). Accordingly, some characteristics regarding the soil pore structure could be revealed by the spatial change in local hydraulic conductivity (k_{k-j}) along the seepage path, as shown in Fig. 13. Note that the normalized local hydraulic conductivity in the figure means the ratio between local and global hydraulic conductivities, and the hydraulic conductivity can be derived from the data in Fig. 10 based on Darcy's law.

Fig. 12 Spatial–temporal evolution characteristics of local hydraulic gradients of the specimen FC30-D75-C100 with internal erosion time
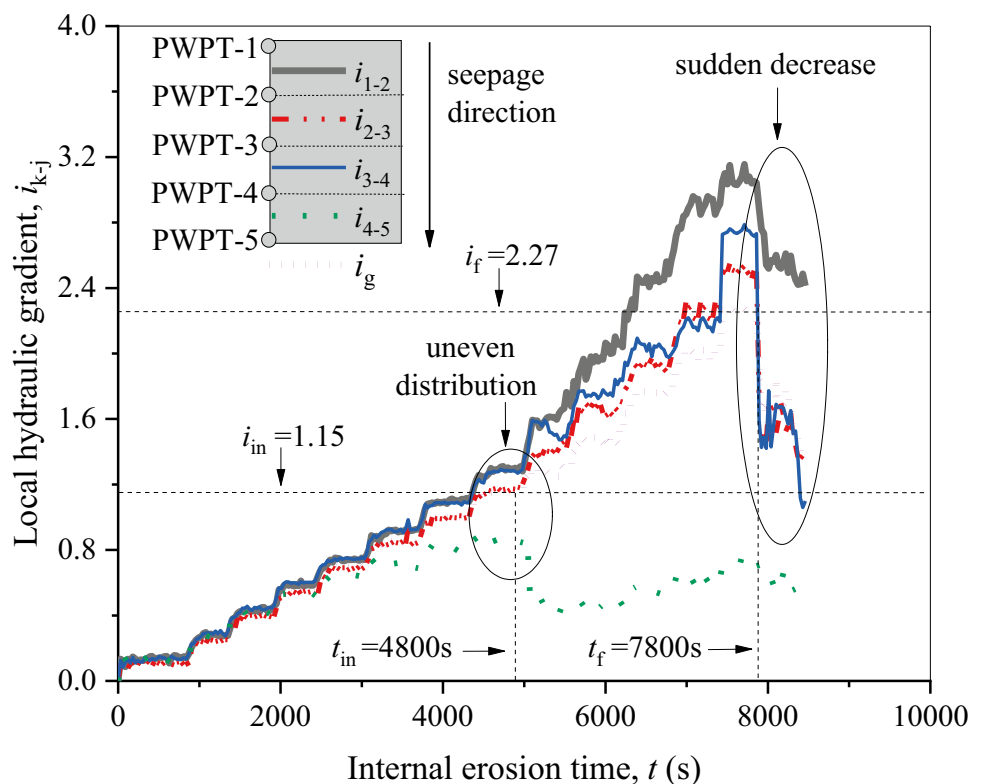
From Fig. 12, before the initiation hydraulic gradient, the local hydraulic gradients increased approximately linearly with lasted internal erosion time and were basically the same as each other. This observation implied that the soil specimen was initially homogenous due to well-controlled specimen preparation. Correspondingly, the normalized local hydraulic conductivity of the specimen FC30-D75-C100 at the initial state (i.e., i_0 in Fig. 13) was approximately equal to 1. The local and global hydraulic conductivities were approximately the same, implying that the soil pore structure was homogenous. After the internal erosion initiation (test lasted to 4800 s), the local hydraulic gradients exhibited nonuniform distribution along the seepage path (see Fig. 12), which became more significant with increasing internal erosion time. For example, the relationship between the global hydraulic gradient and local hydraulic gradients was $i_{1-2} > i_{3-4} > i_{2-3} \approx i_g > i_{4-5}$ at a given internal erosion time. The results suggested a heterogeneous alteration in the soil pore structure due to the difference in the migration and loss of fine particles along the seepage path. This alteration could be evidenced by the normalized local hydraulic conductivity of the specimen FC30-D75-C100. Under the initiation state (e.g., i_{in} in Fig. 13), the normalized local hydraulic conductivity fluctuated around 1. When the applied hydraulic gradient exceeded the failure hydraulic gradient (test lasted to 7800 s), both the global and local hydraulic gradients decreased sharply (see Fig. 12). Correspondingly, the seepage velocity increased drastically (see Fig. 5), and abundant fine particles were flushed out. The fluctuation in normalized local hydraulic conductivity of the specimen FC30-D75-C100 at the failure state (e.g., i_f in Fig. 13) was significant, particularly near both the upstream and downstream portions. The observations implied that some connected pore channels for fine particles had been formed within the soil specimen, resulting in the internal erosion failure.

In short, the spatial and temporal evolution of local hydraulic gradients indicated that the soil specimen might gradually become more heterogeneous along the seepage path due to the migration and loss of movable fine particles after the internal erosion initiation. Furthermore, with the progress of internal erosion, the heterogeneity characteristics of soil specimens became significant. From this perspective, some important observations characterizing the internal erosion might be better evaluated by the captured local responses rather than the global hydraulic gradient of soil specimens. Although the local hydraulic gradients were obtained by Moffat and Fannin (2011) and Benamar et al. (2019), only a rigid-wall permeameter was used in their conducted internal

Fig. 13 Normalized local hydraulic conductivity along the seepage path of the specimen FC30-D75-C100
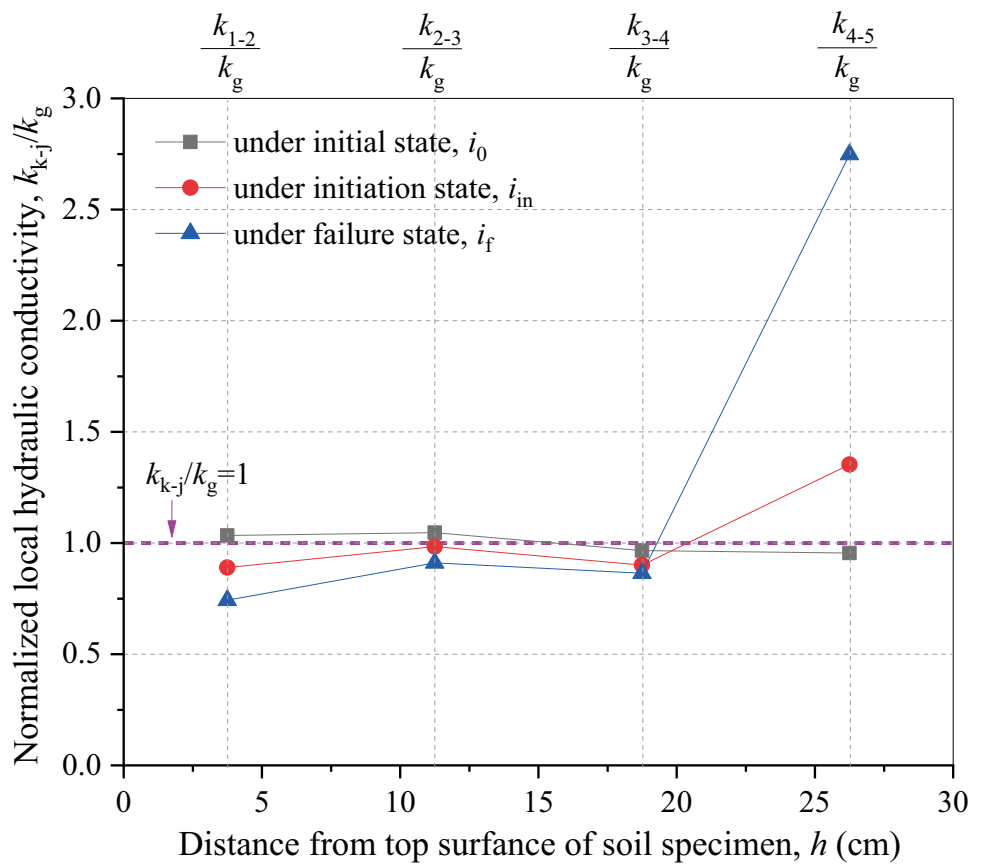
erosion tests. Thus, based on this study, in future follow-up work, a microscopic approach (e.g., tomographic imaging and mercury intrusion porosimetry) will be used before and after the internal erosion tests to obtain more information on the soil pore structure and the local heterogeneity of soil.

Evolution of volumetric and axial and radial deformations as well as void ratio

Figure 14 shows the evolution of cumulative volumetric deformation with a cumulative erosion rate of fine particles (E_c) under different effective confining stresses. Note that the change in the total volume of soil specimens is measured by water exchange in the standard pressure/volume controller during the internal erosion process. From Fig. 14, soil specimens exhibited a volume shrinkage phenomenon (i.e., positive volumetric strains, referred to as ε_v) induced by internal erosion under effective confining stress. The reason might be attributed to the weakening of lateral support of the soil skeleton due to the loss of fine particles involved in force chains, coupled with the particle rearrangement induced by the migration of fine particles. As a result, a contractive behavior was induced during the internal erosion process. Ke and Takahashi (2014a) and Sato and Kuwano (2018) also reported that the loss of fines might weaken lateral supports provided by the fine particles to force chains, resulting in similar contractive behavior. For each

case, the ε_v increased nonlinearly with the E_c value. Under the small applied hydraulic gradient (i.e., $i_g < i_{in}$), no fine particles were eroded, while the small volumetric strains might have been induced by seepage extrusion (Jiang et al. 2013) and jet flow effects (Ke and Takahashi 2014a; Prasomsri and Takahashi 2021). Both seepage extrusion and jet flow effects might be affected by effective confining stress and decrease with increasing effective confining stress. The observation might be attributed to the smaller size of soil pores under higher effective confining stress (see Table 3), which weakened the effect of seepage flow on the soil skeleton. Similar results were found in the experimental study by Ke and Takahashi (2014a). After the internal erosion initiation, the loss of fine particles resulted in a mutation of volume shrinkage, exhibiting a significant increase in volumetric strains. Furthermore, the smaller soil pores could increase the erosion resistance of soil specimens and make it more difficult for the migration and loss of fine particles, exhibiting a significant decrease in E_c (see Fig. 9). The soil skeleton was stronger due to firmer interlocking between coarse and fine particles under higher effective confining stress. Thus, the volumetric strains decreased significantly with the increase in effective confining stress, as shown in Fig. 14.

Furthermore, the axial and radial deformations during the internal erosion process were measured using the photographic method (see Fig. 3) proposed by Chen et al. (2017).

Fig. 14 Volumetric deformation versus cumulative erosion rate of fine particles under different confining stresses for the specimen with 30% initial fine content
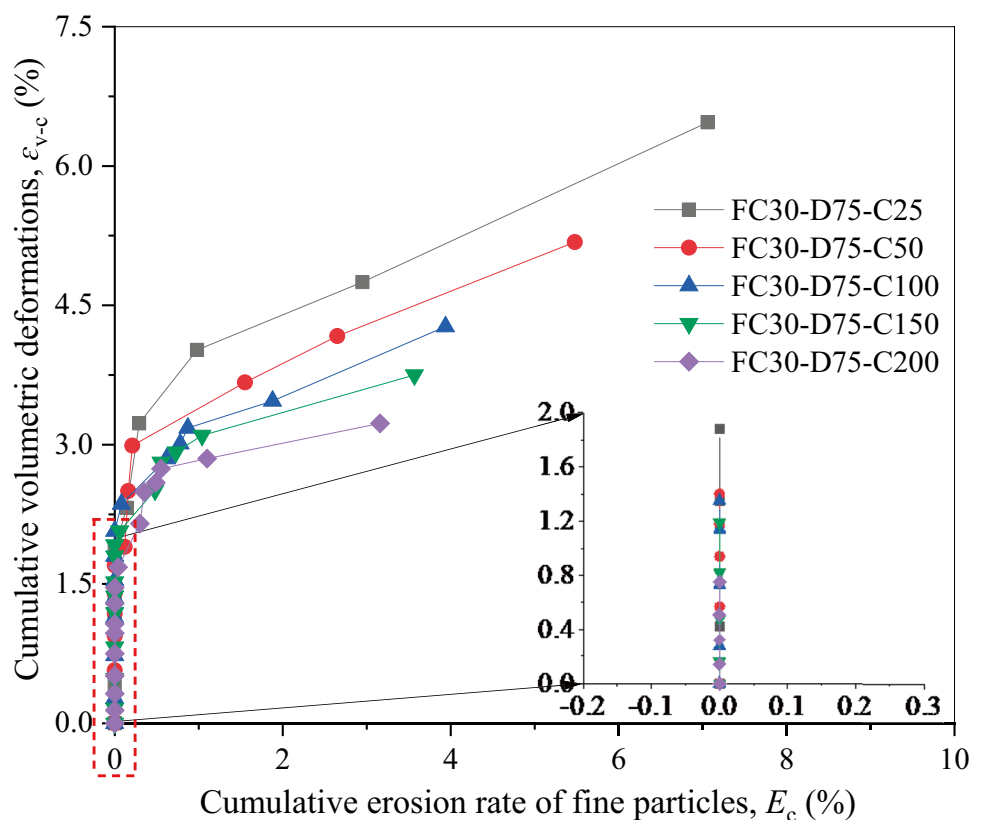
Correspondingly, the void ratio (e) was calculated according to the method proposed by Ke and Takahashi (2014a), which could consider the loss of fine particles and volumetric deformations. Taking the specimen FC30-D75-C100 as an example, Fig. 15 shows the evolution of the axial and radial strains (referred to as ε_a and ε_r, where positive value means a decrease in high and diameter of the soil specimen), as well as the void ratio with internal erosion time. From Fig. 15, both the volumetric and axial strains increased with internal erosion time. Radial strains near upstream, middle, and downstream portions of the soil specimen exhibited similar observations. The observations were consistent with the results found by Ke and Takahashi (2014a). They also reported that the continuous loss of fines might result in an evident increase in the radial strains.

As shown in Fig. 15, after the initiation of hydraulic gradient (i.e., i_{in}), fine particles began to be flushed out, leading to a mutation of the soil specimen in terms of deformations and void ratio. The pore structure along the seepage path might be heterogeneous due to the difference in the migration distance and replenishment condition of fine particles. As a result, at a given internal erosion time, the downstream radial strain ($\varepsilon_{r\text{-downstream}}$) was the largest, followed by the upstream radial strain ($\varepsilon_{r\text{-upstream}}$), and the radial strain near the middle portion ($\varepsilon_{r\text{-middle}}$) was the smallest. Internal erosion tests conducted by Yang and Kuwano (2017) and Sato and Kuwano (2018) also found a difference in the deformations between upstream and downstream portions due to the internal erosion-induced heterogeneity of the soil specimen. Note that the loss of fine particles released the pore volume, while the volume shrinkage behavior reduced the pore volume of the soil specimen. Thus, the void ratio during the internal erosion process might be affected by both the loss of fine particles and volumetric deformations of the soil specimen. In this study, although the soil specimen subjected to confining stress exhibited volume shrinkage during internal erosion, the post-erosion void ratio increased (see Fig. 15) due to the dominant effect of fine particle loss on the soil pores.

Implication for solving engineering practice with internal erosion problems

According to the global and local responses of soil subjected to internal erosion under confining stress, the following points are noted to advance the understanding of internal erosion regarding the fundamental behavior and evaluate the health status of hydraulic geo-structures with internal erosion problems:

1. Soil may gradually become more heterogeneous along the seepage path due to the migration and loss of fine particles after the internal erosion initiation. The nonuniform distribution of local hydraulic gradients may be considered a sign of the occurrence of the local heterogeneity of the soil induced by internal erosion, exhibiting that the local

Fig. 15 Evolution of soil deformations (ε_v, ε_a and ε_r) and void ratio of the specimen FC30-D75-C100 with internal erosion time
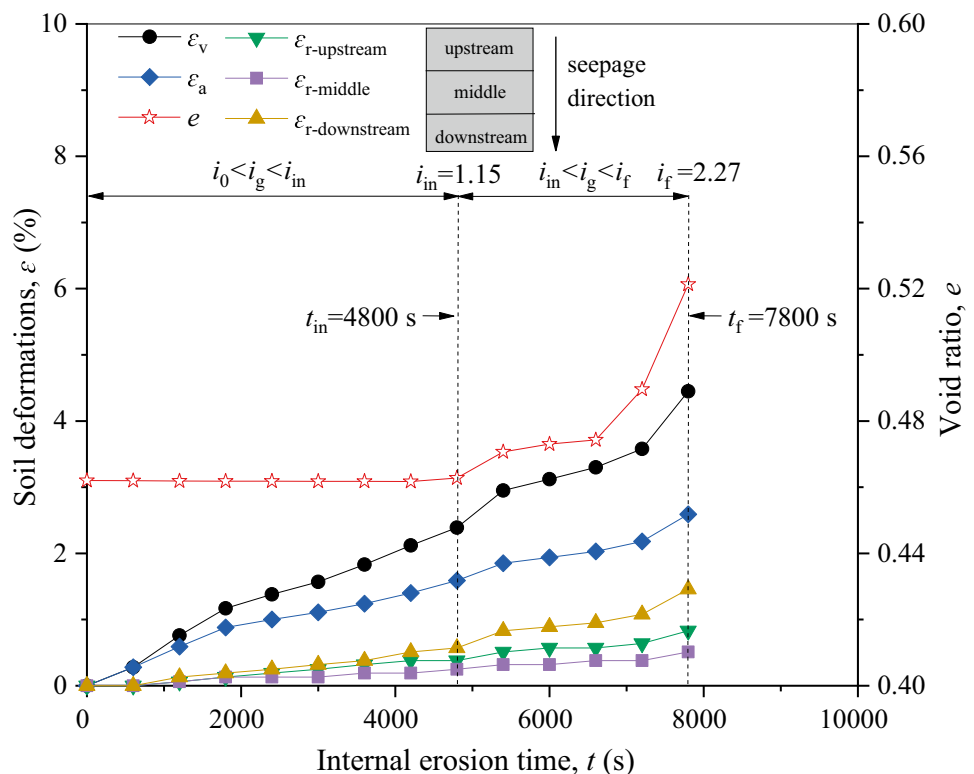
hydraulic gradients somewhere along the seepage path are lower or higher than the global hydraulic gradient.

2. In engineering practice, potential local overpressures frequently occur in soil, and hence, the local hydraulic gradients should be captured for solving internal erosion problems in the hydraulic geo-structures. This is crucial for hydraulic geo-structures as the excessive increase of local hydraulic gradients may aggravate the internal erosion-induced heterogeneity of the soil. Accordingly, the health status of hydraulic geo-structures suffering from internal erosion may be better evaluated using the local responses.

Conclusions

In this study, the effects of confining stress on the global and local responses of internal erosion were investigated by a series of internal erosion tests on gap-graded cohesionless soils using a triaxial permeameter with measurable local hydraulic gradients and deformations. In all tests, the gap-graded cohesionless soil specimens with 30% initial fine content subjected to the effective confining stress within 200 kPa were used, serving as the application conditions of the tests. The main conclusions are as follows:

1. Confining stress effect on the internal erosion of gap-graded cohesionless soil is significant, exhibiting the change in the pattern of internal erosion progression and a nonlinear increase in both the initiation and failure hydraulic gradients as confining stress increases. Specifically, the development of seepage velocity exhibits a two-stage linear progression with increasing applied hydraulic gradient under lower confining stress, while it exhibits a single-stage linear progression under higher confining stress.

2. With increasing confining stress, the cumulative loss of fine particles is decreased significantly, and internal erosion initiation and failure time are delayed. The cumulative loss of fine particles nonlinearly increases with the progress of internal erosion under confining stress. With the cumulative loss of fine particles, the volumetric deformations of the soil specimens are nonlinear, and the post-erosion void ratio increases due to the dominant effect of fine particle loss on soil pores.

3. Spatial and temporal evolution of local hydraulic gradients and local hydraulic conductivity as well as deformations indicates that the soil specimens becomes more heterogeneous along the seepage path due to the migration and loss of fine particles after the internal erosion initiation. As confining stress increases, the onset of nonuniform distribution of local hydraulic gradients along the seepage path is delayed, implying the enhancement of soil erosion resistance.

4. Soil specimens subjected to confining stress exhibits a volume shrinkage phenomenon due to internal erosion, and higher confining stress leads to lower volumetric deformation. The mutation of the soil specimen in terms of volumetric, axial, and radial deformation as well as void ratio may be induced when fine particles begin to be flushed out during the internal erosion process.

Declarations

References

ASTM D4767-11 (2011) Standard test method for consolidated undrained triaxial compression test for cohesive soils Annual Book of ASTM Standards ASTM International, West Conshohocken

ASTM D2487-17 (2017) Standard practice for classification of soils for engineering purposes (Unified Soil Classification System) Annual Book of ASTM Standards ASTM International, West Conshohocken

Benamar A, Correia dos Santos RN, Bennabi A, Karoui T (2019) Suffusion evaluation of coarse-graded soils from Rhine dikes. Acta Geotech 14(3):815–823. https://doi.org/10.1007/s11440-019-00782-1

Bendahmane F, Marot D, Alexis A (2008) Experimental parametric study of suffusion and backward erosion. J Geotech Geoenviron Eng 134(1):57–67. https://doi.org/10.1061/(ASCE)1090-0241(2008)134:1(57)

Burenkova VV (1993) Assessment of suffusion in non-cohesive and graded soils. Filters in Geotechnical and Hydraulic Engineering. Brauns, Heibaum and Schuler, Balkema, Rotterdam, pp 357–360

Chang DS, Zhang LM (2011) A stress-controlled erosion apparatus for studying internal erosion in soils. Geotech Test J 34(6):579–589. https://doi.org/10.1520/GTJ103889

Chang DS, Zhang LM (2013a) Critical hydraulic gradients of internal erosion under complex stress states. J Geotech Geoenviron Eng 139(9):1454–1467. https://doi.org/10.1061/(ASCE)GT.1943-5606.0000871

Chang DS, Zhang LM (2013b) Extended internal stability criteria for soils under seepage. Soils Found 53(4):569–583. https://doi.org/10.1016/j.sandf.2013.06.008

Chen C, Zhang LM, Zhu H (2017) A photographic method for measuring soil deformations during internal erosion under triaxial stress conditions. Geotech Test J 41(1):43–54. https://doi.org/10.1520/GTJ20170031

Chen R, Liu L, Li Z, Deng G, Zhang Y (2021) A novel vertical stress-controlled apparatus for studying suffusion along horizontal seepage through soils. Acta Geotech 16(7):2217–2230. https://doi.org/10.1007/s11440-021-01164-2

Deng G, Zhang LL, Chen R, Liu LL, Shu KX, Zhou ZL (2020) Experimental investigation on suffusion characteristics of cohesionless soils along horizontal seepage flow under controlled vertical stress. Front Earth Sci 8:195. https://doi.org/10.3389/feart.2020.00195

EM 1110–2–2300 (2004) General design and construction considerations for earth and rock-fill dams. U.S. Army Corps of Engineers. Washington, DC, pp 20314–1000

Fannin RJ, Moffat R (2006) Observations on internal stability of cohesionless soils. Geotechnique 56(7):497–500. https://doi.org/10.1680/geot.56.7.497

Huang D, Huang WB, Ke CY, Song YX (2021) Experimental investigation on seepage erosion of the soil-rock interface. Bull Eng Geol Environ 80(4):3115–3137. https://doi.org/10.1007/s10064-021-02104-w

Indraratna B, Israr J, Li M (2018) Inception of geohydraulic failures in granular soils-an experimental and theoretical treatment. Geotechnique 68(3):233–248. https://doi.org/10.1680/jgeot.16.P.227

Israr J, Indraratna B (2019) Study of critical hydraulic gradients for seepage-induced failures in granular soils. J Geotech Geoenviron Eng 145(7):04019025. https://doi.org/10.1061/(ASCE)GT.1943-5606.0002062

Jiang ZM, Wang w, Feng SR, Zhong HY (2013) Experimental of study the relevance between stress state and seepage failure of sandy-gravel soil. Shuili Xuebao 44(12):1498–1505. https://doi.org/10.13243/j.cnki.slxb.2013.12.014

Ke L, Takahashi A (2012) Strength reduction of cohesionless soil due to internal erosion induced by one-dimensional upward seepage flow. Soils Found 52(4):698–711. https://doi.org/10.1016/j.sandf.2012.07.010

Ke L, Takahashi A (2014a) Experimental investigations on suffusion characteristics and its mechanical consequences on saturated cohesionless soil. Soils Found 54(4):713–730. https://doi.org/10.1016/j.sandf.2014.06.024

Ke L, Takahashi A (2014b) Triaxial erosion test for evaluation of mechanical consequences of internal erosion. Geotech Test J 37(2):347–364. https://doi.org/10.1520/GTJ20130049

Kenney TC, Lau D (1985) Internal stability of granular filters. Can Geotech J 22(2):215–225. https://doi.org/10.1139/t85-029

Kézdi A (1979) Soil physics: selected topics-developments in geotechnical engineering. Elsevier Science Ltd., Amsterdam, Netherlands

Khaksar Najafi E, Eslami A (2015) Assessment of the likelihood of suffusion in alluvial soils: case history. Bull Eng Geol Environ 74(2):611–620. https://doi.org/10.1007/s10064-014-0681-x

Kuwano R, Santa Spitia LF, Bedja M, Otsubo M (2021) Change in mechanical behaviour of gap-graded soil subjected to internal erosion observed in triaxial compression and torsional shear. Geomech Energy Envir 27:100197. https://doi.org/10.1016/j.gete.2020.100197

Li ML, Zhang XC, Yang ZJ, Yang T, Pei XJ (2020) The rainfall erosion mechanism of high and steep slopes in loess tablelands based on experimental methods and optimized control measures. Bull Eng Geol Environ 79(9):4671–4681. https://doi.org/10.1007/s10064-020-01854-3

Liang Y, Zeng C, Wang JJ, Liu MW, Yeh TCJ, Zha YY (2017) Constant gradient erosion apparatus for appraisal of piping behavior in upward seepage flow. Geotech Test J 40(4):630–642. https://doi.org/10.1520/GTJ20150282

Liang Y, Yeh TCJ, Chen Q, Xu W, Hao Y (2019) Particle erosion in suffusion under isotropic and anisotropic stress states. Soils Found 59(5):1371–1384. https://doi.org/10.1016/j.sandf.2019.06.009

Liu WP, Wan SF, Huang FM, Luo XY, Fu MF (2019) Experimental study of subsurface erosion in granitic under the conditions of different soil column angles and flow discharges. Bull Eng Geol Environ 78(8):5877–5888. https://doi.org/10.1007/s10064-019-01519-w

Liu K, Qiu RZ, Su Q, Ni PP, Liu B, Gao J, Wang TF (2021) Suffusion response of well graded gravels in roadbed of non-ballasted high speed railway. Constr Build Mater 284:122848. https://doi.org/10.1016/j.conbuildmat.2021.122848

Luo YL, Jin X, Li X, Zhan ML, Sheng JC (2013) A new apparatus for evaluation of contact erosion at the soil-structure interface. Geotech Test J 36(2):256–263. https://doi.org/10.1520/GTJ20120094

Luo Y, Luo B, Xiao M (2020) Effect of deviator stress on the initiation of suffusion. Acta Geotech 15(6):1607–1617. https://doi.org/10.1007/s11440-019-00859-x

Mao CX (2005) Study on piping and filters: part I of piping. Rock Soil Mechanics 26(2):209–215. https://doi.org/10.16285/j.rsm.2005.02.008

Marot D, Tran DM, Bendahmane F (2020) Multidirectional flow apparatus for assessing soil internal erosion susceptibility. Geotech Test J 43(6):1481–1498. https://doi.org/10.1520/GTJ20190254

Milligan V (2003) Some uncertainties in embankment dam engineering. J Geotech Geoenviron Eng 129(9):785–797. https://doi.org/10.1061/(ASCE)1090-0241(2003)129:9(785)

Moffat RA, Fannin RJ (2006) A large permeameter for study of internal stability in cohesionless soils. Geotech Test J 29(4):273–279. https://doi.org/10.1520/GTJ100021

Moffat R, Fannin RJ (2011) A hydromechanical relation governing internal stability of cohesionless soils. Can Geotech J 48(3):413–424. https://doi.org/10.1139/T10-070

Moffat RA, Fannin RJ, Garner SJ (2011) Spatial and temporal progression of internal erosion in cohesionless soil. Can Geotech J 48(3):399–412. https://doi.org/10.1139/T10-071

Pachideh V, Mir Mohammad Hosseini SM (2019) A new physical model for studying flow direction and other influencing parameters on the internal erosion of soils. Geotech Test J 42(6):1431–1456. https://doi.org/10.1520/GTJ20170301

Prasomsri J, Takahashi A (2020) The role of fines on internal instability and its impact on undrained mechanical response of gap-graded soils. Soils Found 60(6):1468–1488. https://doi.org/10.1016/j.sandf.2020.09.008

Prasomsri J, Takahashi A (2021) Experimental study on suffusion under multiple seepages and its impact on undrained mechanical responses of gap-graded soil. Soils Found 61(6):1660–1680. https://doi.org/10.1016/j.sandf.2021.10.003

Razavi SK, Hajialilue Bonab M, Dabaghian A (2020) Investigation into the internal erosion and local settlement of Esfarayen Earth-Fill Dam. J Geotech Geoenviron Eng 146(4):04020006. https://doi.org/10.1061/(ASCE)GT.1943-5606.0002216

Richards KS, Reddy KR (2007) Critical appraisal of piping phenomena in earth dams. Bull Eng Geol Environ 66(4):381–402. https://doi.org/10.1007/s10064-007-0095-0

Richards KS, Reddy KR (2010) True triaxial piping test apparatus for evaluation of piping potential in earth structures. Geotech Test J 30(1):83–95. https://doi.org/10.1520/GTJ102246

Sato M, Kuwano R (2015) Suffusion and clogging by one-dimensional seepage tests on cohesive soil. Soils Found 55(6):1427–1440. https://doi.org/10.1016/j.sandf.2015.10.008

Sato M, Kuwano R (2018) Laboratory testing for evaluation of the influence of a small degree of internal erosion on deformation and stiffness. Soils Found 58(3):547–562. https://doi.org/10.1016/j.sandf.2018.01.004

Skempton AW, Brogan JM (1994) Experiments on piping in sandy gravels. Geotechnique 44(3):449–460. https://doi.org/10.1680/geot.1994.44.3.449

Terzaghi K (1939) Soil mechanics: a new chapter in engineering science. J Instn Civ Eng 12:106–141. https://doi.org/10.1680/ijoti.1939.14534

Tian DL, Xie Q, Fu X, Zhang JH (2020) Experimental study on the effect of fine contents on internal erosion in natural soil deposits. Bull Eng Geol Environ 79(8):4135–4150. https://doi.org/10.1007/s10064-020-01829-4

Vallejo LE (2001) Interpretation of the limits in shear strength in binary granular mixtures. Can Geotech J 38(5):1097–1104. https://doi.org/10.1139/cgj-38-5-1097

Wan CF, Fell R (2008) Assessing the potential of internal instability and suffusion in embankment dams and their foundations. J Geotech Geoenviron Eng 134(3):401–407. https://doi.org/10.1061/(ASCE)1090-0241(2008)134:3(401)

Yang Y, Kuwano R (2017) Effects of principal stress rotation on small strain stiffness of sand subjected to piping erosion. Soils Found 57(5):776–788. https://doi.org/10.1016/j.sandf.2017.08.008

Yuan G, Che A (2022) Evolution and spatio-temporal characteristics of slope erosion due to rainfall in Southwest China. Bull Eng Geol Environ 81(7):1–18. https://doi.org/10.1007/s10064-022-02767-z

Zhang LL, Wu F, Zhang H, Zhang J (2019) Influences of internal erosion on infiltration and slope stability. Bull Eng Geol Environ 78(3):1815–1827. https://doi.org/10.1007/s10064-017-1185-2

Zhang LL, Deng G, Chen R, Zhang YQ, Luo ZY (2023) Experimental investigation on evolution process of suffusion in gap-graded cohesionless soil. Chin J Geotech Eng 45(7):1412–1420. https://doi.org/10.11779/CJGE20220468

Zhong C, Le VT, Bendahmane F, Marot D, Yin ZY (2018) Investigation of spatial scale effects on suffusion susceptibility. J Geotech Geoenviron Eng 144(9):04018067. https://doi.org/10.1061/(ASCE)GT.1943-5606.0001935

Zhou ZQ, Ranjith PG, Li Z (2018) An experimental testing apparatus for study of suffusion of granular soils in geological structures. Tunn Undergr Space Tech 78:222–230. https://doi.org/10.1061/(ASCE)1532-3641(2005)5:3(218)